

# Trends, noise and reentrant long-term persistence in Arctic sea ice

S. Agarwal<sup>1,2</sup>, W. Moon<sup>2</sup>, & J. S. Wettlaufer<sup>2,3,4,5</sup>

<sup>1</sup>*Department of Mathematics, Indian Institute of Technology Guwahati, Guwahati 781 039, Assam, India*

<sup>2</sup>*Department of Geology and Geophysics, Yale University, New Haven, Connecticut 06520, USA*

<sup>3</sup>*Department of Physics, Yale University, New Haven, Connecticut 06520-8109, USA*

<sup>4</sup>*Program in Applied Mathematics, Yale University, New Haven, Connecticut 06520, USA*

<sup>5</sup>*NORDITA, Roslagstullsbacken 23, SE-10691 Stockholm, Sweden*

(Dated: January 26, 2023)

We examine the long-term correlations and multifractal properties of daily satellite retrievals of Arctic sea ice albedo and extent, for periods of  $\sim 23$  years and 32 years respectively. The approach used is a recent development called Multifractal Temporally Weighted Detrended Fluctuation Analysis (MF-TWDFA), which exploits the intuition that in any time series points closer in time are more likely to be related than distant points. This is expressed by application of weighted moving windows—points nearer each other are weighted more than those farther away—to determine the function used to fit the time series *profile*; the running sum of the raw data. This offers several advantages over the commonly used MF-DFA. Firstly, in MF-DFA the *profile* of the time series is fit using discontinuous polynomials, which can introduce errors in the determination of crossover times for new scalings, with a particular relevance at long time scales. Secondly, for time series of length  $N$ , MF-DFA is typically informative only up to  $N/4$  whereas MF-TWDFA can be carried out to  $N/2$ . Finally, the generalized fluctuation functions  $F_q(s)$  for all moments  $q$  as a function of time scale  $s$  are substantially smoother for all  $s$  and this is markedly so for large values. This facilitates clear extraction of crossover times from one scaling to another. We determine the generalized Hurst exponents and multiple crossover timescales from synoptic to decadal with several between. The method reveals these in both data sets and hence provides a quantitative basis for analysis of geophysical responses to climate forcing that goes beyond treatments that assume a single decay scale process, such as a first-order autoregressive process, which cannot be justifiably fit to such observations. Most importantly, the strength of the seasonal cycle is such that it “masks” long term correlations on time scales beyond seasonal. When removing the seasonal cycle from the original record, the ice extent data exhibits a white noise behavior from seasonal to bi-seasonal time scales, but the clear fingerprints of the short (weather) and long ( $\sim 7$  and 9 year) time scales remain. Therefore, (i) long term persistence is reentrant beyond the seasonal scale and (ii) it is not possible to distinguish whether a given ice area minimum (maximum) will be followed by a minimum (maximum) that is larger or smaller in magnitude.

PACS numbers: 05.45.Df, 92.10.Rw, 92.70.Gt, 05.45.-a

## I. INTRODUCTION

Earth’s polar oceans are viewed as a bellwether of climate change because their surfaces are covered by a thin (several meters) mosaic of high albedo sea ice floes that modulate the atmosphere/ocean heat flux. Whence, as opposed to the massive meteoric ice sheets that are several kilometers thick, sea ice is considered to be more sensitive component of the cryosphere to perturbations and feedbacks, particularly the ice-albedo feedback which has driven large scale climate events over Earth history [1]. For example, the retreat of Arctic sea ice coverage during recent decades (Fig. 1) has captured substantial interest [2, 3]. An essential question concerns the nature of the decay in ice coverage; is it a trend associated with the influence of greenhouse forcing, or is it a fluctuation in a quantitative record that is short ( $\sim 30$  years) relative to the dynamics of the cryosphere on climatic epochs ( $\gtrsim 10^6$  yrs)?

Both past climate data and basic physical arguments indicate that a sufficiently large increase in greenhouse gas concentration will drive decay in the ice cover, whereas the state of the art global climate models under-project the observed recent decay [2]. However, Tietsche et al., [4] numerically prescribed ice-free summer states at various times during the projection of 21<sup>st</sup> century climates and found that ice extent

typically recovered within several years. Whilst such rapid response times can be captured within the framework of relatively simple theory [5], both internal and external forcings and their intrinsic time scales manifest themselves in large scale observations of the geophysical state of the system. Due to the fact that we cannot *a-priori* exclude the observed decline in the ice cover as being an intrinsic decadal oscillation or nonstationary influence in the climate system, we use the finest temporal resolution in the observed record to examine the action of multiple scales. The fingerprints of the noisy dynamics of the system on time scales longer than the seasonal record may reside in that record itself, and our goal here is to extract these and interpret those we can in light of the underlying processes that may have left them. It is hoped that the approach will provide guidelines for theoretical and numerical modeling efforts, as well as comparative data analysis studies.

Most observational studies of the satellite records of ice coverage extrapolate in time the annual or monthly means (e.g., see Fig. 1 of [3]). Whilst the observed declines over this troika of decades, particularly the last decade, are striking our goal here is to begin a systematic effort to distinguish between long term correlations and trends in this finite record. In so doing we examine whether there exists a multiplicity of persistent scales in the data that can provide a basis for examining cause and effect in the geophysical scale observables of the system. Therefore, we view several types of large-scale

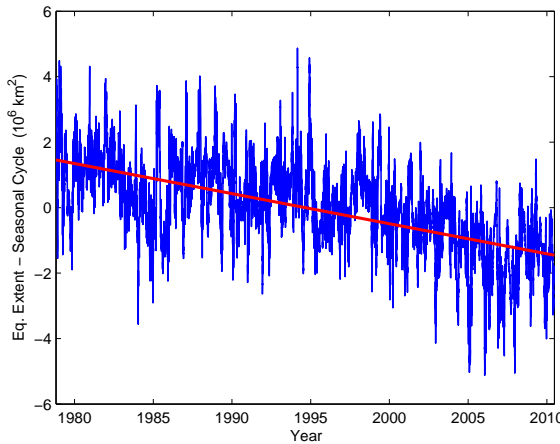


FIG. 1: Equivalent Ice Extent (EIE) during the satellite era (blue) shown relative to the mean (red) with the seasonal cycle removed. EIE, which differs from traditional ice extent or ice area, is defined as the total surface area, including land, north of the zonal-mean ice edge latitude, and thus is proportional to the sine of the ice edge latitude. EIE was defined by Eisenman [13] to deal with the geometric muting of ice area associated with the seasonal bias of the influence of the Arctic basin land mass boundaries. Here we use EIE and hence refer to it either via this acronym or simply ice extent.

sea ice data as a multifractal system in which a spectrum of scaling—the singularity spectrum—characterizes the behavior of nearby points [6, 7]. The basic approach of relevance is the multi-fractal generalization of Detrended Fluctuation Analysis (DFA) advanced and widely applied by Kantelhardt and colleagues [8, 9] aptly called Multifractal Detrended Fluctuation Analysis (MF-DFA). In the last decade this approach has been developed in many directions, from studying extreme events with nonlinear long term memory [10], to examining the influence of additive noise on long term correlations (e.g., [11]). Here we use a new extension of this methodology called Multifractal Temporally Weighted Detrended Fluctuation Analysis (MF-TWDFA), which exploits the intuition that in any time series points closer in time are more likely to be related than distant points and can provide a rather more clear signature of long time scales in the fluctuation function and its moments [12]. In the next section we summarize MF-TWDFA and describe its connection to the conventional approaches of analyzing autocorrelation functions and power spectra. The geophysical data are described in Section III after which we present the principal results from MF-TWDFA in Section IV before concluding.

## II. MULTIFRACTAL TEMPORALLY WEIGHTED DETRENDED FLUCTUATION ANALYSIS (MF-TWDFA)

Here, we harness a new variant of MF-DFA to study the long-range correlations and fractal scaling properties of time series data of basin wide Arctic sea ice area and satellite albedo retrievals. The new variant, called multifractal tempo-

rally weighted detrended fluctuation analysis (MF-TWDFA), was developed by Zhou and Leung [12] and uses weighted regression to express the intuition that points closer in time are more likely to be similar than those that are more distant. To insure that this paper is reasonably self contained we motivate the approach by first discussing the general rationale for multifractals versus the treatment of time series using autocorrelations and spectral analysis. We then describe MF-DFA followed by a development of the aspects that distinguish MF-TWDFA from MF-DFA.

### A. Rationale for a multifractal approach

Consider a time series of length  $i, \dots, N$  describing a quantity  $X_i$ . The linear two-point autocorrelation function  $C(s)$  for realizations of  $X_i$  separated by an increment  $s$  is given by

$$C(s) = \frac{1}{\sigma_X^2(N-s)} \sum_{i=1}^{N-s} (X_i - \bar{X}_i) (X_{i+s} - \bar{X}_i), \quad (1)$$

in which  $\sigma_X^2$  is the variance and  $\bar{X}_i$  is the mean. When  $C(s) \propto s^{-\gamma}$ , the mean correlation time  $\mathcal{T}_s \equiv \int_0^N C(s) ds$  diverges as  $N \rightarrow \infty$  for  $0 < \gamma < 1$  and the time series is said to exhibit *long-term persistence*; on average the linear correlations become arbitrarily long (e.g., see [7]). Whereas, when  $\gamma \geq 1$  we have finite  $\mathcal{T}_s$  and hence the  $X_i$  are *short-term correlated*. Finally, when  $C(s) = 0$  for  $s > 0$  then the  $X_i$  are *uncorrelated*. Therefore, there may be a time  $s^*$  that delimits correlated from uncorrelated  $X_i$  viz.,  $C(s < s^*) > 0$  and  $C(s > s^*) = 0$ .

Despite the simplicity of characterizing a system using a single scaling exponent  $\gamma$  it has long been understood that a wide range of natural and laboratory systems have correlations that cannot be captured by such an approach [6, 7]. It is particularly important to extract the scaling behavior for the long-term correlations, wherein the variability on long time scales may be poorly represented by a single scaling exponent and long-term trends or periodicity may obscure the calculation of the autocorrelation function. Moreover, the distinction between trends and long-term correlations in stationary time series can become blurred. These comprise some of the reasons for the introduction of a multifractal description of the correlations which replaces a single value with a continuous spectrum of scaling exponents.

### B. Multifractal detrended fluctuation analysis

There are four stages in the implementation of MF-DFA [8]. Firstly, one constructs a nonstationary *profile*  $Y(i)$  of the original time series  $X_i$ , which is the cumulative sum

$$Y(i) \equiv \sum_{k=1}^i (X_k - \bar{X}_k), \quad \text{where } i, \dots, N. \quad (2)$$

Secondly, the profile is divided into  $N_s = \text{int}(N/s)$  segments of equal length  $s$  that do not overlap. Excepting rare circumstances, the original time series is not an exact multiple of  $s$  leaving excess segments of  $Y(i)$ . These are dealt with by repeating the procedure from the end of the profile and returning to the beginning and hence creating  $2N_s$  segments. Thirdly, within each of the  $\nu = 1, \dots, 2N_s$  segments the variance  $\text{Var}(\nu, s)$  of the profile relative to a local least squares polynomial fit  $y_\nu(i)$  of  $n^{\text{th}}$  order is

$$\text{Var}(\nu, s) \equiv \frac{1}{s} \sum_{i=1}^s [Y([\nu - 1]s + i) - y_\nu(i)]^2. \quad (3)$$

Finally, the generalized fluctuation function is formed as

$$F_q(s) \equiv \left[ \frac{1}{2N_s} \sum_{\nu=1}^{2N_s} \{\text{Var}(\nu, s)\}^{q/2} \right]^{1/q}, \quad (4)$$

and the principal tool of MF-DFA is to examine how  $F_q(s)$  depends on the choice of time segment  $s$  for a given degree of polynomial fit  $n$  and the order  $q$  of the moment taken. The scaling of the generalized fluctuation function is characterized by a generalized Hurst exponent  $h(q)$  viz.,

$$F_q(s) \propto s^{h(q)}. \quad (5)$$

When the time series is monofractal then  $h(q)$  is independent of  $q$  and is thus equivalent to the classical Hurst exponent  $H$ . For the case of  $q = 2$ , MF-DFA and DFA are equivalent [8]. Whence, a time series with long-term persistence has  $h(2) = 1 - \gamma/2$  for  $0 < \gamma < 1$ , whereas short-term correlated data, decaying faster than  $1/s$ , has  $\gamma > 1$  and finite  $\mathcal{T}_s$  leading to a crossover at  $s = s^*$  and asymptotic behavior defined by  $h(2) = 1/2$ . Moreover, the connection between  $h(2)$  and the

decay of the power spectrum  $S(f) \propto f^{-\beta}$ , with frequency  $f$  is  $h(2) = (1 + \beta)/2$  [e.g., 14]. Therefore, one sees that for classical white noise,  $\beta = 0$  and hence  $h(2) = 1/2$ , whereas for Brownian or red noise  $\beta = 2$  and  $h(2) = 3/2$ .

In general multifractal time series exhibit a scaling dependence on the moment  $q$ . Hence, one can relate the generalized Hurst exponents to the Renyi exponents  $\tau(q)$  of the partition function approach to multifractals [7], viz.,  $\tau(q) = h(q)q - 1$  where the singularity spectrum  $f(\alpha) \equiv q\alpha - \tau(q)$  with  $\alpha \equiv d\tau(q)/dq$  describes the dimension of the subset of the  $X_i$  characterized by a Hölder exponent (or singularity strength)  $\alpha$ . Finally,  $\tau(q) \equiv (q-1)D_q$ , where  $D_q$  is the generalized set of dimensions of Hentschel and Procaccia [15] (see also [16]), constitutes a different characterization of the fractal properties of a system; knowing  $D(q)$  allows one to determine all correlation functions of points on an attractor. Complimentary approaches are useful because multifractality can originate both in a broad probability density as well as large and small fluctuations having a different long-term persistence. The MF-DFA procedure can distinguish between these [8] so that different exponents provide tests of distinct multifractal origins.

### C. Moving Windows and MF-TWDFA

The generalization of MF-DFA by Zhou and Leung [12] applies a variant of the weighted least squares approach to fitting the polynomial  $y_\nu(i)$  to the profile  $Y(i)$  on each interval  $\nu$ . Here, rather than using  $n^{\text{th}}$  order  $y_\nu(i)$ 's to estimate  $Y(i)$  *within* a fixed window, without reference to points in the profile outside that window, a moving window which is smaller than  $s$  but determined by distance between points is used to construct a point by point approximation  $\hat{y}_\nu(i)$  to the profile. Thus, instead of Eq. 3 we compute the variance up ( $\nu = 1, \dots, N_s$ ) and down ( $\nu = N_s + 1, \dots, 2N_s$ ) the profile as

---


$$\begin{aligned} \text{Var}(\nu, s) &\equiv \frac{1}{s} \sum_{i=1}^s \{Y([\nu - 1]s + i) - \hat{y}([\nu - 1]s + i)\}^2 & \text{for } \nu = 1, \dots, N_s \\ \text{Var}(\nu, s) &\equiv \frac{1}{s} \sum_{i=1}^s \{Y(N - [\nu - N_s]s + i) - \hat{y}(N - [\nu - N_s]s + i)\}^2 & \text{for } \nu = N_s + 1, \dots, 2N_s. \end{aligned} \quad (6)$$


---

Therefore we replace the global linear regression of fitting the polynomial  $y_\nu(i)$  to the data as appears in Eq. (3), with a weighted local estimate  $\hat{y}_\nu(i)$  determined by the proximity of points  $j$  to the point  $i$  in the time series such that  $|i - j| \leq s$ . A larger (or smaller) weight  $w_{ij}$  is given to  $\hat{y}_\nu(i)$  according to whether  $|i - j|$  is small (large).

In the ordinary least squares method one minimizes the sum of the squared differences between the predicted and the original function, whereas in weighted least squares a weight factor is applied to the squared differences before performing the minimization. There are many varieties of weighted least squares originating in time series analysis for evenly spaced observations [17] and “robust” locally weighted regression for unevenly spaced data [18]. The standard weighted linear regression scheme fits observed variables  $Y(i)$  and  $\mathcal{X}_k(i)$  as-

suming a linear relationship as

$$Y(i) = a_0(i) + \sum_{k=1}^m a_k(i) \mathcal{X}_k(i) + \epsilon(i), \quad (7)$$

where  $\epsilon(i)$  is the error, which may (but need not) be homoscedastic. Here,  $a_k(i)$  is the  $k^{\text{th}}$  fitting parameter at time  $i$ , the vector  $\mathbf{a}$  of which is determined from

$$\mathbf{a} = (\mathcal{X}^T \mathbf{w} \mathcal{X})^{-1} \mathcal{X}^T \mathbf{w} \mathbf{Y}, \quad (8)$$

where  $\mathbf{w}$  is a diagonal matrix with weight elements  $w_{ij}$  with magnitudes that depend on the proximity to  $i$  thereby estimating an  $a_k(i)$  according to a prescribed criterion of proximity.

Hence,  $\hat{y}_\nu(i)$  is determined by a weighted least squares approach using

$$\hat{y}_\nu(i) = a_0(i) + a_1(i)i + \epsilon(i), \quad i, \dots, N. \quad (9)$$

Here again the fitting parameters  $a(i) = [a_0(i), a_1(i)]^T$  depend on the place  $i$  in the series and are determined from equation (8) in which the  $w_{ij}$ , with  $j = 1, \dots, n$ , are the diagonals of an  $n \times n$  diagonal matrix, and  $\mathcal{X}$  is an  $n \times 2$  matrix with the first column being unity and the second running from 1 to  $n$ . We use the same bisquare function for the weights

$$w_{ij} = \begin{cases} \left(1 - \left[\frac{|i-j|}{s}\right]^2\right)^2, & \text{if } |i-j| \leq s, \\ 0, & \text{otherwise,} \end{cases} \quad (10)$$

as did Zhou and Leung [12], although one can envisage a range of possibilities for dealing with the temporal weighting.

We conclude this section by emphasizing that a principal advantage of MF-TWDFA over conventional MF-DFA is the robustness of extracting the scaling of the fluctuation function, and hence the crossover points between scalings, that indicate the underlying processes reflected in the data. Of particular importance is the fidelity of extracting the long-term scaling behavior in geophysical data sets which can often be obscured in MF-DFA and, as we shall see, compromises MF-TWDFA when a strong seasonal cycle remains in the original time series.

### III. SEA ICE GEOPHYSICAL DATA

We use MF-TWDFA to examine the multi-scale structure of two satellite based geophysical data sets for Arctic sea ice; the Equivalent Ice Extent (EIE) and albedo retrievals from the Advanced Very High Resolution Radiometer (AVHRR) Polar Pathfinder (APP) archive. The EIE data derives from retrievals of satellite passive microwave radiances over the Arctic converted to daily sea ice concentration using the NASA Team Sea Ice Algorithm in the same manner as described by Eisenman [13], who focused on the origin of the difference between ice extent and EIE. We refer to the reader to Eisenman's paper for a detailed description of the determination of EIE. The mean EIE seasonal cycle from 1978-present is shown in Fig. 2. Daily satellite retrievals of the directional - hemispheric apparent albedo are determined from the APP archive as described in a separate publication dedicated to a different form of analysis than presented here [19]. The apparent albedo is what would be measured by upward and downward looking radiometers and thus varies with the state of the atmosphere and the solar zenith angle.

The APP dataset has been refined for use in a wide range of polar studies and is described in detail in [19, and refs. therein]. In brief, the AVHRR channels range from the visible to the thermal infrared (0.58 - 12.5  $\mu\text{m}$ ) and measure top of the atmosphere reflectances and brightness temperatures. With 5 km  $\times$  5 km resolution, we analyze albedo retrievals from 1 January 1982 through 31 December 2004, taken daily

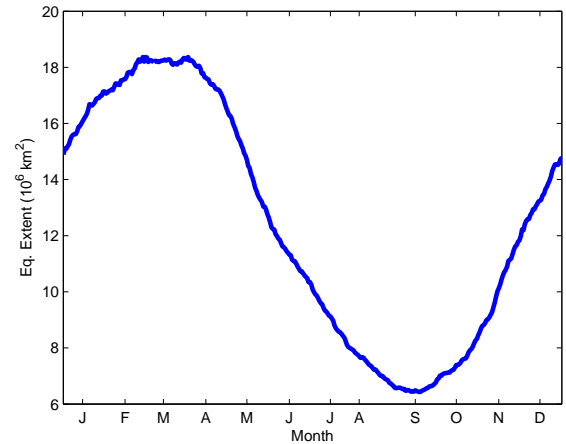


FIG. 2: The mean seasonal cycle of the Equivalent Ice Extent (EIE) during the satellite era. See also figure 1.

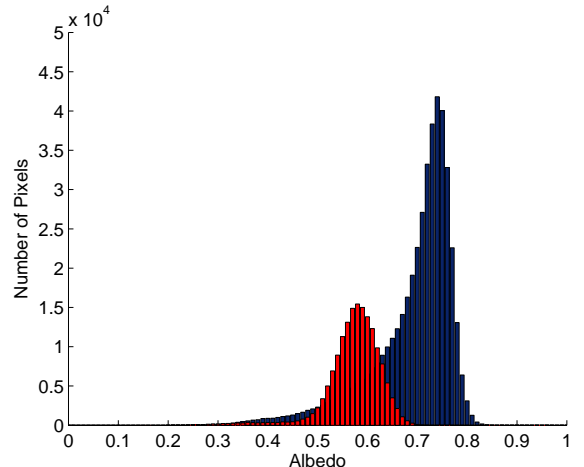


FIG. 3: The albedo histograms shown for days in mid-March (blue) and -September (red). If there is ice in a pixel for the 23 year duration of the data set then we compute the albedo for that pixel and average over all pixels that have met this criterion [19]

at 1400 hours. Sea ice is distinguished from land and open water using microwave brightness temperatures and filtering the Surface Type Mask data with the NASA Team Sea Ice Algorithm which distinguishes between first-year (FYI) and multi-year ice (MYI) concentrations. The approach ascribes a MYI flag to a region containing at least 50 percent of this ice type, with uncertainties depending on the season (e.g., melt pond fraction) and region (near the ice edge), along with the surface type categories. On physical grounds the albedo data are filtered to remove any values greater than 1 or less than 0.2. Each pixel is assessed every day for the presence of ice and then albedo is averaged for that pixel [19]. Examples of histograms for mid-March and mid-September are shown in Fig. 3.

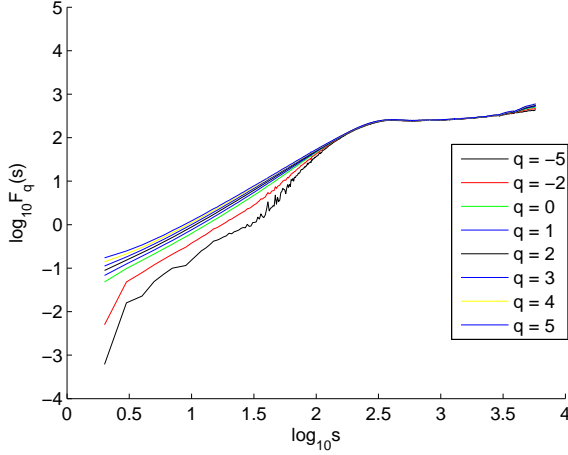


FIG. 4: The fluctuation function from equation (5) for the Equivalent Ice Extent (EIE) *with a seasonal cycle*. The  $q$ 's are shown in the panel and  $s$  is measured in days throughout.

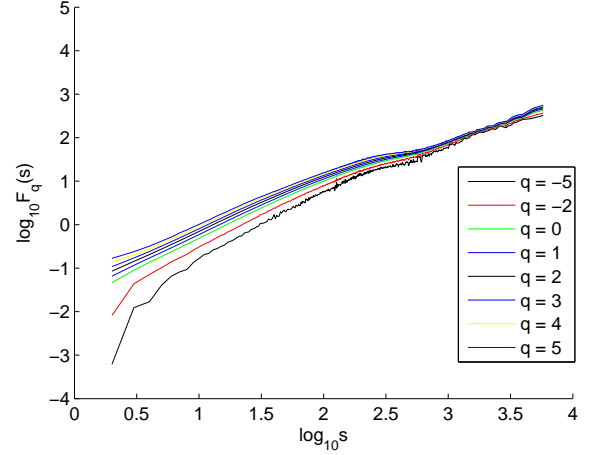


FIG. 6: The fluctuation function from equation (5) for Equivalent Ice Extent (EIE) *without a seasonal cycle*. The  $q$ 's are shown in the panel.

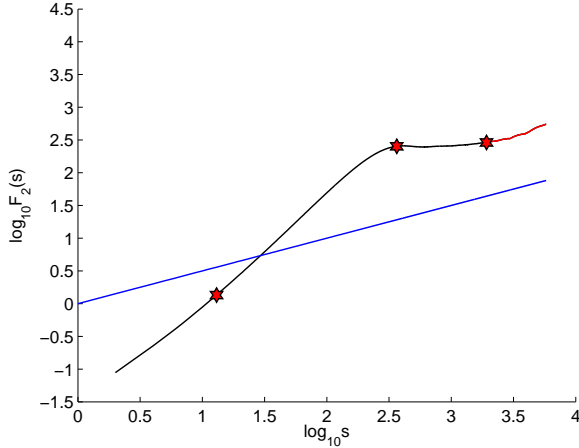


FIG. 5: The fluctuation function from equation (5) for Equivalent Ice Extent (EIE) *with a seasonal cycle* for  $q=2$ . The stars denote the times associated with a slope change at approximately 13 days, 1 year and 5.25 years. The blue line and the red segment of the black curve both denote white noise with  $h(2) = 1/2$ .

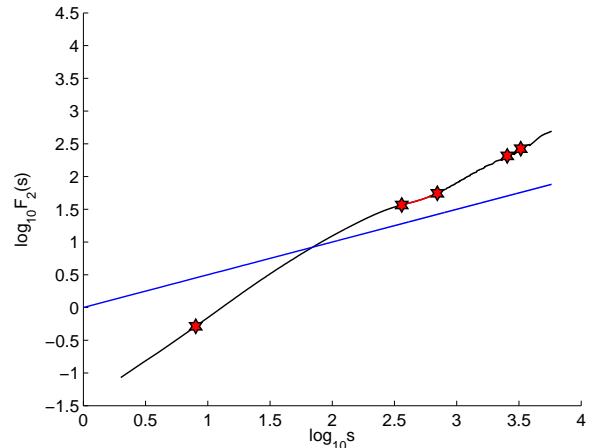


FIG. 7: The fluctuation function from equation (5) for Equivalent Ice Extent (EIE) *without a seasonal cycle* for  $q=2$ . The stars denote the times associated with a slope change at approximately 8 days, 1 year, 2 years, 6.9 years and 8.9 years. The blue line and the red segment of the black curve both denote white noise with  $h(2) = 1/2$ .

#### IV. RESULTS AND DISCUSSION

Here we focus most of our discussion on the nature of the fluctuation functions  $F_q(s)$  that emerge from MF-TWDFA and return later to the exponents, generalized dimensions and singularity spectra. First, we note that we have eliminated the possibility of spurious multi-fractality [20] by checking the usual measures  $\Delta h_{20} \equiv h(-20) - h(20)$  and  $\Delta \alpha$ . Second, whilst we show the fluctuation functions for a range of  $q$ , for clarity we also show plots solely for  $q = 2$  and remind the reader that for  $h(2) = 1/2$  the system exhibits a completely uncorrelated white noise dynamics, and for  $h(2) = 3/2$  there are red (or Brownian) noise correlations. Whereas for  $0 < h(2) < 1/2$  the dynamics are anticor-

lated. Moreover, as noted above, for analysis by power spectra  $\beta = 2h(2) - 1$ . It is understood within this multifractal framework that small temporal fluctuations are characterized by  $h(q)$ 's for  $q < 0$  whereas large temporal fluctuations are characterized by  $h(q)$ 's for  $q > 0$ . As we discuss below the fluctuation functions  $F_q(s)$  do indeed distinguish the scaling of small and large fluctuations. As a test of the fidelity of the many crossovers in slope (associated with particular intrinsic time scales) detected with MF-TWDFA, we applied *both* MF-DFA and MF-TWDFA. We found that the crossovers for time scales of 2 years or longer would not have been captured by MF-DFA because of large amplitude fluctuations in this range. Note, for the EIE data with a seasonal cycle this result was confirmed for polynomial fitting in the detrending step

of MF-DFA of up to order 9, while for the other data up to order 3. Moreover, and that which we focus on here, the MF-TWDFA analysis used on the time series after removing the seasonal cycle leads to the extraction of crossovers associated with long term persistence that are “masked” when the seasonal cycle is not removed. This finding is discussed in more detail presently.

### A. Masking long term correlations by strong seasonal cycle

A prominent feature of our analysis is the role played by the seasonal cycle. This is the origin of the striking distinction between Figs. 4, 5 and 6, 7 for the EIE and Figs. 10, 11 and 12, 13 for the albedo. It is seen that the strength of the seasonal cycle is such that it “masks” the dynamics on time scales longer than seasonal thereby suppressing the fingerprints of long term persistence. This is clearly displayed in the fluctuation functions. Firstly, in Figs. 4 and 10, which have a seasonal cycle, we see that the curves for all  $q$ ’s converge at the 1 year time scale. This convergence is removed when the seasonal cycle is removed as seen in Figs. 6 and 12. Secondly, when the original time series still possesses the seasonal cycle, the slope abruptly drops below  $h(2) = 1/2$  at the 1 year time scale to transition to an anticorrelated structure. This behavior is distinct from the clear transitions and positive slopes at longer time scales that are seen when the seasonal cycle is removed from the original time series (Figs. 6, 7, 12, 13). Whilst there is a finite union of underlying processes that influence the ice extent and the ice albedo, that union is clearly not one to one [19]. Thus, although we find *some* similar qualitative structure in the analysis of the EIE and albedo data with and without a seasonal cycle, there are important quantitative distinctions. For example, the high frequency weather time scales of order week’s are clearly seen in all of the data. However, Figs. 5 and 11 clearly show masking beginning at one year, the transition to anticorrelated behavior and then a steeper–white noise–slope of  $h(2) = 1/2$  returning at 5 and 2.2 years respectively. Whence, all long term persistence is destroyed by the strength of the seasonal cycle which can be seen to be associated with the strong periodicity remaining in the profiles of Fig. 8. Although we see that the general steep/flat/steep behavior of the slopes of the fluctuation function with increasing time is shared between Figs. 5, 11 and Figs. 7, 13, the essential distinction is that in the latter case—with the seasonal cycle removed—long term persistence is reentrant. Indeed, time scales of  $\sim 7$  and 9 years are seen in both the EIE and albedo data.

Most importantly, the region between 1 and 2 years in the EIE data without a seasonal cycle shows  $h(2) \approx 1/2$ . In other words, although the strength of the seasonal cycle is such that it dominates the power spectrum (not shown), when removing the seasonal scale from the original EIE data the system exhibits a white noise behavior from the seasonal to the bi-seasonal time scales. However, the clear fingerprints of the short (weather) and long ( $\sim 7$  and 9 year) time scales remain. The implications of this finding are, unfortunately for the goal of forecasting, rather clear; a given ice minimum

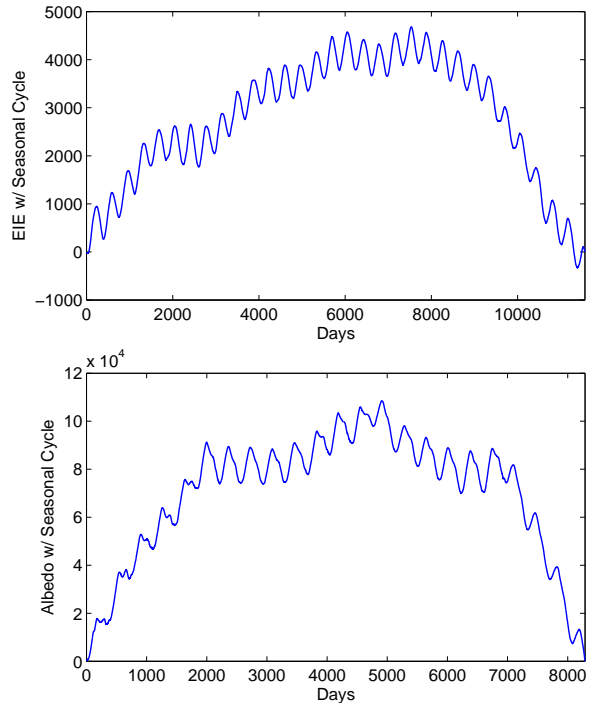


FIG. 8: The profiles for the EIE (top) and Albedo from Eq. 2 with a seasonal cycle in the original time series.

(maximum) can be followed by a minimum (maximum) with a larger or smaller magnitude. The same logic follows for minima/maxima separated by two years and the EIE states on time scales between. Most of the discussion in the literature focuses on the extremes in the observations (maxima and minima) which we find here to exhibit a nearly white time distribution. If we interpret the results in the limit  $h(2) = 1/2$  then the autocorrelation will have strong peaks at the seasonal maxima, minima and bi-seasonal maxima and minima with rapid decays for times from one to two years. As discussed below, this is consistent with aspects of other studies in which rapid decorrelations are found.

It is important to be clear regarding what the results *do not* tell us. We are not saying that existence of minima or maxima (or states between) are uncorrelated in time, but solely that the magnitudes of those states cannot be predicted to be larger or smaller from these data alone. Moreover, the lack of an extended autocorrelation does not a-priori constrain the probability distribution associated with the process from which the value of the observable originates, but rather solely refers to the temporal distribution of the observable. In other words one probability distribution can underly the nature of how a given magnitude of the EIE or albedo is reached and the temporal distribution of those magnitudes is white on seasonal to bi-seasonal time scales. Thus, on such time scales these data are *short-term correlated*, are associated with a finite  $\mathcal{T}_s$  and an autocorrelation that decays faster than  $\sim s^{-1}$ . Therefore, the processes controlling the EIE or albedo states in the Arctic are the familiar regular strong seasonal scale radiative and advective forcings. This is explained by the robustness

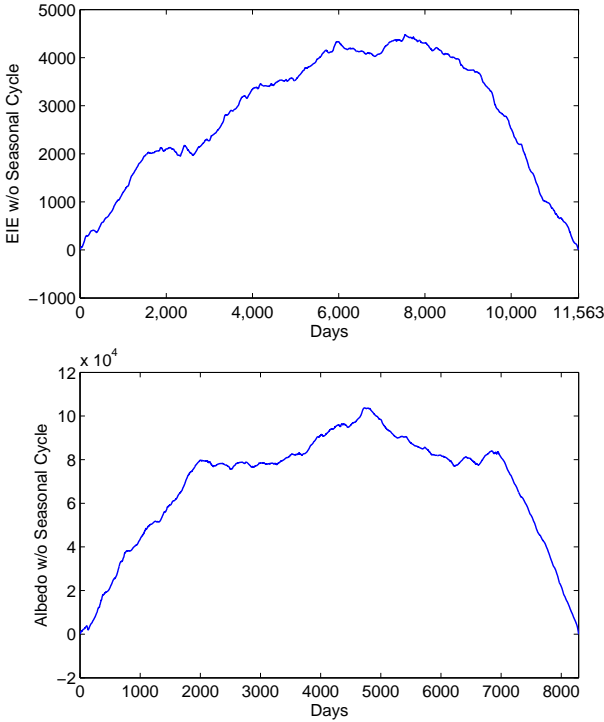


FIG. 9: The profiles for the EIE (top) and Albedo from Eq. 2 removing the seasonal cycle from the original time series.

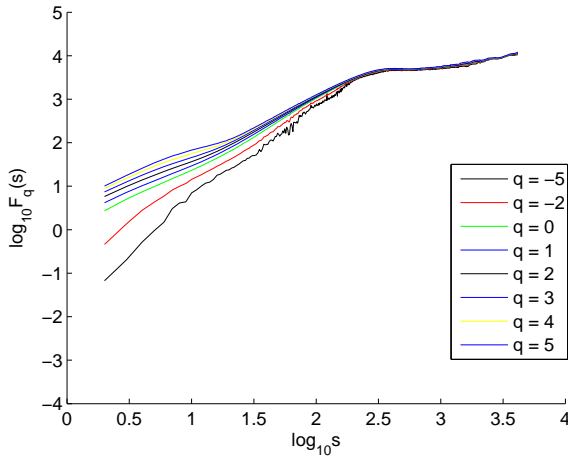


FIG. 10: The fluctuation function from equation (5) for the ice albedo with a seasonal cycle. The  $q$ 's are shown in the panel.

of the response times associated with the seasonal control of the ice state through the competition between the ice-albedo feedback in summer and the long-wave forcing in winter [5]. With further retreat of the ice cover we expect then that the associated trend might have the influence of increasing the  $h(2)$  above 1/2 associated with longer term influences on the magnitude of the ice state although this may be counteracted by a higher degree of noise in the state of the system.

The longer time scales of  $\sim 7$  and 9 years found here with a

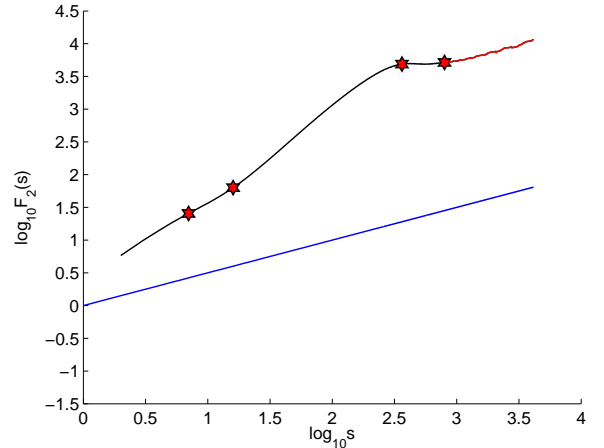


FIG. 11: The fluctuation function from equation (5) for ice albedo with a seasonal cycle for  $q=2$ . The stars denote the times associated with a slope change at approximately 7 days, 16 days, 1 year and 2.2 years. The blue line and the red segment of the black curve both denote white noise with  $h(2) = 1/2$ .

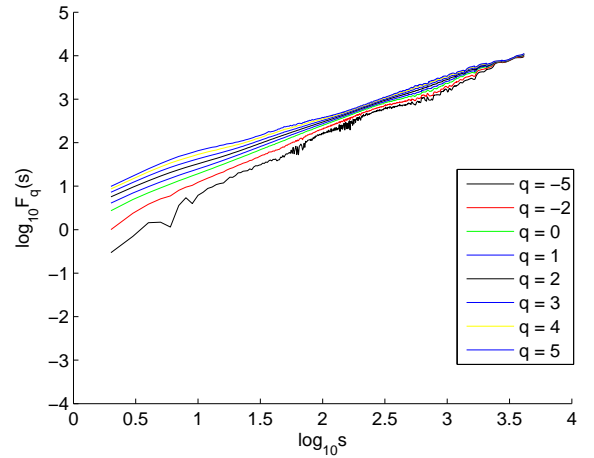


FIG. 12: The fluctuation function from equation (5) for the ice albedo without a seasonal cycle. The  $q$ 's are shown in the panel.

steeper slope we could casually ascribe to the overall decay of the ice cover [13] and the associated processes associated with albedo variability as the ice cover thins [19]. We leave for future analysis what would likely be a less quantitative endeavor to correlate these longer time scales with climate indices that have time scales ranging from 2 to 7 years (for the El Niño Oscillation) to a decade or many decades (such as for the Pacific Decadal, North Atlantic or the Arctic Oscillations). It is however important to note that dynamical processes acting over decadal scales can be extracted from this analysis and it may be that the rapid decline in the ice coverage during the most recent decade is dominating the crossover found here.

Figs. 14, 15 and 16, 17 show  $h(q)$ , the slope of the fluctuation curve, for each  $q$  and is calculated as the slope of the linear approximation of the entire curve. It is thus principally

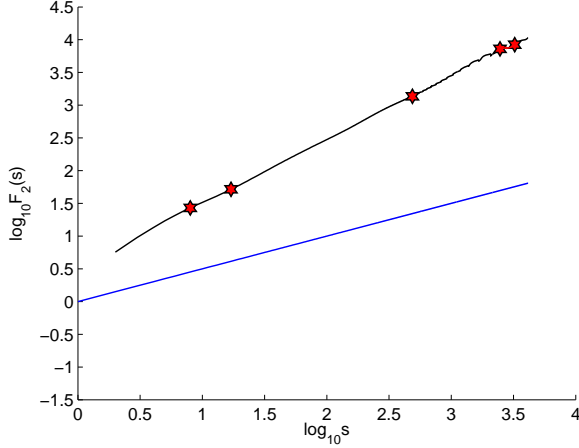


FIG. 13: The fluctuation function from equation (5) for ice albedo *without a seasonal cycle* for  $q=2$ . The stars denote the times associated with a slope change at approximately 8 days, 17 days, 487 days, 7.5 years and 9 years. The blue line and the red segment of the black curve both denote white noise with  $h(2) = 1/2$ .

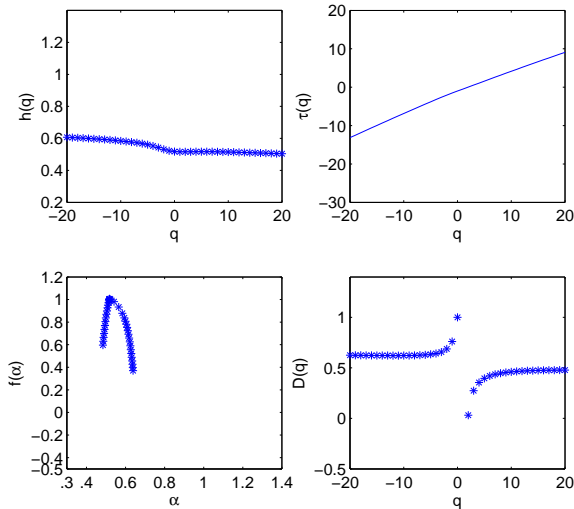


FIG. 14: Equivalent Ice Extent (EIE) *with a seasonal cycle*. The generalized Hurst exponent (upper left), Renyi exponent (upper right) and generalized dimension  $D(q)$  (lower right) as functions of  $q$  with the remaining panel the singularity spectrum  $f(\alpha)$  versus  $\alpha$ .

used here to demonstrate the strong influence of the seasonal cycle which suppresses  $h(q)$  for all  $q$  and thus the crossovers, particularly for long term persistence, as we have seen from the fluctuation functions themselves. The same general behavior is seen with the Renyi exponent's but this is perhaps less pronounced. The singularity spectra with and without the seasonal cycles are strikingly different, displaying that the width of the singularity spectrum  $\Delta\alpha \equiv \alpha_1 - \alpha_2$  (the difference between the maximum  $\alpha_1$  and the minimum  $\alpha_2$  Hölder exponents), distinguishes the degree of multifractality of the

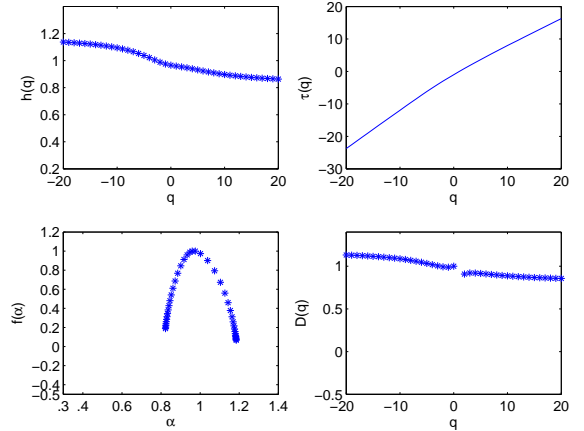


FIG. 15: Equivalent Ice Extent (EIE) *without a seasonal cycle*, the generalized Hurst exponent (upper left), Renyi exponent (upper right) and generalized dimension  $D(q)$  (lower right) as functions of  $q$  with the remaining panel the singularity spectrum  $f(\alpha)$  versus  $\alpha$ .

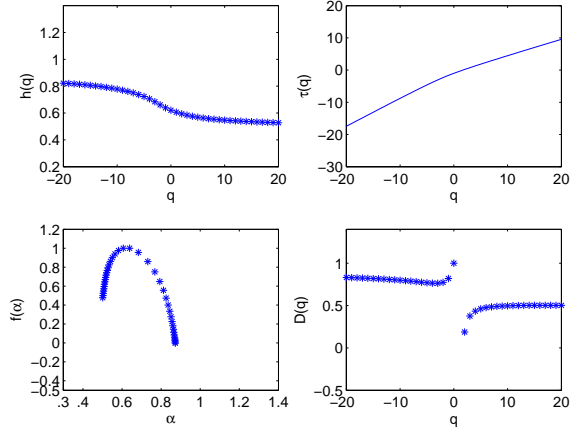


FIG. 16: For the ice albedo with a seasonal cycle, the generalized Hurst exponent (upper left), Renyi exponent (upper right) and generalized dimension  $D(q)$  (lower right) as functions of  $q$  with the remaining panel the singularity spectrum  $f(\alpha)$  versus  $\alpha$ .

seasonal and nonseasonal cycle data. Namely, upon removal of the seasonal cycle from the original time series the value of  $\Delta\alpha$  indicates a transition from bifractal to fully multifractal, which is clearly consistent with the behavior of the fluctuation functions. Moreover, both data sets develop an asymmetric  $f(\alpha)$ . The contrast between multifractality and bi-fractality can be quantified through application of mixing formulae for the Renyi exponent's  $\tau(q)$  [9], and hence the generalized Hurst exponents  $h(q)$ , due to the fact that bi-fractal records can be well characterized by two distinct slopes,  $\alpha_1$  and  $\alpha_2$ , in the following sense.

Variations of the exponent  $\tau(q)$  with different scale values  $q$  form the mass exponent spectrum. This spectrum reveals the system's degree of multi-fractality and nonlinearity [e.g.,

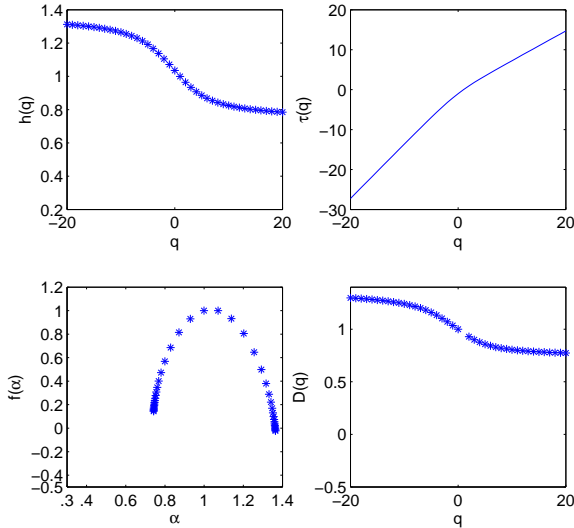


FIG. 17: For the ice albedo without a seasonal cycle, the generalized Hurst exponent (upper left), Renyi exponent (upper right) and generalized dimension  $D(q)$  (lower right) as functions of  $q$  with the remaining panel the singularity spectrum  $f(\alpha)$  versus  $\alpha$ .

6, 7]. For example, a linear  $\tau(q)$  versus  $q$  corresponds to mono-fractal signals and as such all points on the curve belong to the same fractal dimension. Thus, a change in the curvature of  $\tau(q)$  indicates an increasing degree of multifractality, or complexity in its fractal structure. We observe that the  $\tau(q)$  plots in both the EIE and the albedo data with a seasonal cycle are well characterized by two distinct slopes  $\alpha_1$  and  $\alpha_2$ , for values of  $q$  greater (or less) than a crossover value  $q_\otimes$ , which we determine by a fit to the following mixing formulae of Kantelhardt et al. [9] for the Renyi and generalized Hurst exponents;

$$\tau(q) = \begin{cases} q\alpha_1 - 1, & \text{if } q \leq q_\otimes \\ q\alpha_2 + q_\otimes(\alpha_1 - \alpha_2) - 1, & \text{if } q > q_\otimes \end{cases} \quad (11)$$

and hence, because  $\tau(q) = h(q)q - 1$  the associated bi-fractal generalized Hurst exponent is

$$h(q) = \begin{cases} \alpha_1, & \text{if } q \leq q_\otimes \\ q_\otimes(\alpha_1 - \alpha_2)/q + \alpha_2, & \text{if } q > q_\otimes \end{cases}, \quad (12)$$

wherein  $h(q)$  exhibits a plateau from  $q = -\infty$  to  $q_\otimes$  and decays hyperbolically for  $q > q_\otimes$ . We note that the opposite behavior can be obtained from a bifractal model with suitable interchange of the large and small  $q$  behavior [9].

Although this bifractal model requires three parameters, we see that the multifractal spectrum degenerates to two single points, with a width defined by  $\Delta\alpha = \alpha_1 - \alpha_2$  [9]. We fit the EIE and albedo data for  $\alpha_1$ ,  $\alpha_2$  and  $q_\otimes$  and also compute  $\alpha(q = 20) \equiv \alpha_{20}$  and  $\alpha(q = -20) \equiv \alpha_{-20}$  for comparison and the results are shown in Table I. We see important quantitative trends in the table entries. Firstly, the bifractal treatment of the data in which the seasonal cycle remains is rather

Data set	$\alpha_1$	$\alpha_2$	$\Delta\alpha$	$\alpha_{-20}$	$\alpha_{20}$	$\Delta\alpha_{20}$
EIE <sub>wss</sub>	0.612	0.505	0.107	0.638	0.484	0.154
EIE <sub>woss</sub>	1.155	0.863	0.291	1.185	0.823	0.362
Albedo <sub>wss</sub>	0.832	0.531	0.301	0.873	0.501	0.371
Albedo <sub>woss</sub>	1.325	0.799	0.527	1.364	0.742	0.622

TABLE I: The fitted values of  $\alpha_1$ ,  $\alpha_2$  from the bifractal model of Eq. 11 and the values of  $\alpha_{20}$  and  $\alpha_{-20}$  from the full MF-TWDFA results for both EIE and Albedo data. The subscripts wss and woss denote data with the seasonal cycle and without the seasonal cycle. For all bifractal fits  $q_\otimes = -1$  and  $\Delta\alpha_{20} \equiv \alpha_{-20} - \alpha_{20}$

robust, and upon removal of the seasonal cycle the width of the singularity spectrum increases (i.e.  $\Delta\alpha$  and  $\Delta\alpha_{20}$  both increase), and thus the strength of multifractality increases, which is also observed from the fluctuation functions. Secondly, the full MF-TWDFA treatment produces a singularity spectrum width  $\Delta\alpha_{20}$  that better represents the data in which the seasonal cycle is removed in the sense that it more poorly reproduces the bifractal fit;  $\Delta\alpha_{20} - \Delta\alpha$  is larger for EIE<sub>woss</sub> (0.07) and Albedo<sub>woss</sub> (0.1) than for EIE<sub>wss</sub> (0.05) and Albedo<sub>wss</sub> (0.07).

There are distinctions between the plots of the generalized set of dimensions  $D(q)$  for the data with and without the seasonal cycle. Firstly, as expected from the behavior of the  $h(q)$ , the magnitudes of the  $D(q)$  increase upon removal of the seasonal cycle. Secondly, for the case with the seasonal cycle remaining, for large and small values of  $q$  there are asymptotes of nearly constant  $D(q)$  whereas the slopes are finite when the seasonal cycle is removed showing that the dimensions are still converging. Thirdly, for comparison and contrast, we note aspects of the general behavior of a system in which the spectrum of the measure is continuous [16]. The curve  $f(\alpha)$  will be convex and will have one maximum at  $q = 0$  where  $f = D(q = 0) = D_0$ , and  $D_0$  is the set's Hausdorff dimension. Moreover,  $f(\alpha)$  will possess an infinite slope at  $q = \pm\infty$  where  $f = 0$  and  $D_\infty$  and  $D_{-\infty}$  correspond to regions in the fractal set where the measure is most concentrated and most rarefied respectively. However, such behavior may not be exhibited when the measure lies on a continuous support, such as in the case of a generalization of the two-scale Cantor set [16]. In such a case, rather than the most concentrated region of the measure contracting to a point so that  $f = 0$  for  $D_\infty$ , but to a set of points of finite dimension because  $f > 0$  there. This is seen as the asymmetric “hook” like shape of the  $f(\alpha)$  curves, with the smallest value of  $\alpha$ , corresponding to  $D_\infty$ , having finite values. With the exception of EIE<sub>wss</sub> we have  $f = 0$  for  $D_{-\infty}$  and  $f > 0$  for  $D_\infty$  for all cases. The exception has  $f > 0$  for both  $D_{-\infty}$  and  $D_\infty$ . At present we lack a model that predicts the anomalous behavior of  $D(q)$  near the origin when the seasonal cycle remains in the underlying data but ascribe this to the “masking” behavior discussed above.

In his observational analysis of EIE Eisenman [13] noted that the overall retreat of the ice cover is governed by a noisy signal and particularly so at the September minimum. Observations using  $\sim 30$  years of monthly ice extent and area data

show rapid decorrelations of a few months [21] using lag correlation method assuming that the underlying process is a first-order autoregressive process, as was done in a fit of hindcasting simulation output which showed a persistence time scale for September ice area of 1.2 years [22]. In a study of the forecast skill of a linear empirical model Lindsay et al. [23] found no skill in predicting detrended data for time scales of three or more months. Finally, the rapid decay in ice area anomalies is also found in climate models [see 24, and refs therein] and this is argued to underlie the lack of hysteresis associated with the loss of summer sea ice in both global models and theoretical treatments [5, 25].

Although the corpus of these studies lead to the general conclusion of rapidly decaying correlations (which compromise predictability) and are thus heuristically consistent with our interpretation here, there remain important distinctions. Firstly, both data sets as used for this analysis do not explicitly distinguish between the ice types and thus it is not possible here to provide multifractal analysis based on the fraction of the EIE or the albedo that is MYI or FYI. Thus, our analysis applies to the aggregate of the ice cover, whereas, subject to a wide range of caveats, many models can diagnose features such as thickness or type. Secondly, although for context it is simplest to deal with a single moment of the fluctuation function, even that demonstrates the existence of multiple time scales in the data which, as noted in section II A, cannot be treated in a quantitatively consistent manner with a single decay autocorrelation. Moreover, we demonstrated in section IV A that if the seasonal cycle is not removed one will always observe a single crossover time (longer than the synoptic time scale) of 1 year; a time scale at which all moments converge. Thus, if the time resolution of a study is more coarse than synoptic, an upper bound on the persistence time on any study that assumes an autoregressive process with a lag of one year will inevitably be  $\sim 1$  year, as is indeed found for ice area [21, 22]. Apart from the single moment evidence of multiple scales in the system, the approach here highlights the dangers of not carefully detrending the seasonality and dealing with stationarity.

## V. CONCLUSIONS

We have examined the long-term correlations and multifractal properties of daily satellite retrievals of Arctic sea ice albedo and ice areal extent, for periods of  $\sim 23$  years and 32 years respectively, with and without the seasonal cycle removed. A recent development called Multifractal Temporally Weighted Detrended Fluctuation Analysis (MF-TWDFA), which exploits the intuition that in any time series

points closer in time are more likely to be related than distant points, was adapted for use with these data. Points in the records nearer each other are weighted more than those farther away in order to determine the polynomial used to fit the time series *profile*, which is a cumulative product of the time series. As a methodology the approach offers several advantages over the more generally applied MF-DFA. Firstly, in MF-DFA the profile of the time series is fit using discontinuous polynomials, which can introduce errors in the determination of crossover times for new scalings, and can be particularly questionable at long time scales. Secondly, for time series of length  $N$ , whilst MF-DFA is typically informative only up to  $N/4$ , MF-TWDFA can be carried out to  $N/2$ . Finally, the generalized fluctuation functions  $F_q(s)$  for all moments  $q$  as a function of time scale  $s$  are substantially smoother for all  $s$  and this is particularly so for large values. This facilitates clear extraction of crossover times from one scale to another. The generalized Hurst exponents and multiple crossover timescales were found to range from the synoptic or weather time scale to decadal, with several between. Such multiple time scales were exhibited in both data sets and hence the approach provides a framework to examine ice dynamical and thermodynamical responses to climate forcing that goes beyond treatments that assume a process involving a single autocorrelation decay, such as a first-order autoregressive process. Indeed, the method shows that single decay autocorrelations cannot be meaningfully fitted to these geophysical observations. Our most important finding is that the strength of the seasonal cycle is such that it dominates the power spectrum and “masks” long term correlations on time scales beyond seasonal. When removing the seasonal scale from the original record, the EIE data exhibits a white noise behavior from the seasonal to the bi-seasonal time scales, but the clear fingerprints of the short (weather) and long ( $\sim 7$  and 9 year) time scales remain, demonstrating a *reentrant long-term persistence*. Therefore, it is not possible to distinguish whether a given ice area minimum (maximum) will be followed by a minimum (maximum) that is larger or smaller. This means that while it is tempting to use an anomalous excursion associated with a low ice year to predict the following year’s minimum, or that two year’s henceforth, the data do not justify such a prediction.

## Acknowledgments

WM thanks NASA for a graduate fellowship. JSW thanks NORDITA and the Wenner-Gren Foundation for support as a Visiting Professor, the John Simon Guggenheim Foundation and Yale University.

---

[1] B. Saltzman, *Dynamical Paleoclimatology: Generalized Theory of Global Climate Change*, vol. 80 of *International Geophysics Series* (Academic Press, San Diego, 2002).  
 [2] R. Kwok and N. Untersteiner, *Phys. Today* **64**, 36 (2011).  
 [3] M. C. Serreze, *Nature* **471**, 47 (2011).  
 [4] S. Tietsche, D. Notz, J. H. Jungclaus, and J. Marotzke, *Geophys. Res. Lett.* **38**, L02707 (2011).  
 [5] W. Moon and J. S. Wettlaufer, *Europhys. Lett.* **96**, 39001 (2011).  
 [6] H. Stanley and P. Meakin, *Nature* **335**, 405 (1988).

- [7] J. Feder, *Fractals* (Plenum, 1988).
- [8] J. W. Kantelhardt, S. A. Zschiegner, E. Koscielny-Bunde, S. Havlin, A. Bunde, and H. E. Stanley, *Physica A* **316**, 87 (2002).
- [9] J. Kantelhardt, E. Koscielny-Bunde, D. Rybski, P. Braun, A. Bunde, and S. Havlin, *J. Geophys. Res.-Atmos* **111**, D01106 (2006).
- [10] M. I. Bogachev and A. Bunde, *Physica A* **390**, 2240 (2011).
- [11] J. Ludescher, M. I. Bogachev, J. W. Kantelhardt, A. Y. Schumann, and A. Bunde, *Physica A* **390**, 2480 (2011).
- [12] Y. Zhou and Y. Leung, *J. Stat. Mech.: Theor. Exp.* p. P06021 (2010).
- [13] I. Eisenman, *Geophys. Res. Lett.* **37**, L16501 (2010).
- [14] G. Rangarajan and M. Ding, *Phys. Rev. E* **61**, 4991 (2000).
- [15] H. Hentschel and I. Procaccia, *Physica D* **8**, 435 (1983).
- [16] T. Halsey, M. Jensen, L. Kadanoff, I. Procaccia, and B. Shraiman, *Phys. Rev. A* **33**, 1141 (1986).
- [17] F. Macauley, *The Smoothing of Time Series* (National Bureau of Economic Research, New York, 1931).
- [18] W. Cleveland, *J. Amer. Stat. Assoc.* **74**, 829 (1979).
- [19] S. Agarwal, W. Moon, and J. S. Wettlaufer, *Geophys. Res. Lett.* **38**, L20504 (2011).
- [20] A. Y. Schumann and J. W. Kantelhardt, *Physica A* **390**, 2637 (2011).
- [21] E. Blanchard-Wrigglesworth, K. C. Armour, C. M. Bitz, and E. DeWeaver, *J. Climate* **24**, 231 (2011).
- [22] K. C. Armour, C. M. Bitz, L. Thompson, and E. C. Hunke, *J. Climate* **24**, 2378 (2011).
- [23] R. W. Lindsay, J. Zhang, A. J. Schweiger, and M. A. Steele, *J. Geophys. Res.-Oceans* **113**, C02023 (2008).
- [24] K. C. Armour, I. Eisenman, E. Blanchard-Wrigglesworth, K. E. McCusker, and C. M. Bitz, *Geophys. Res. Lett.* **38**, L16705 (2011).
- [25] I. Eisenman and J. S. Wettlaufer, *Proc. Natl. Acad. Sci. USA* **106**, 28 (2009).